# 21 year timing of the black-widow pulsar J2051–0827

G. Shaifullah, J. P. W. Verbiest, P. C. C. Freire, T. M. Tauris, N. Wex, S. Oslowski, B. W. Stappers, C. G. Bassa, R. N. Caballero, D. J. Champion, et al.

# 21 year timing of the black-widow pulsar J2051−0827

G. Shaifullah,[1,2]★ J. P. W. Verbiest,[1,2] P. C. C. Freire,[2] T. M. Tauris,[2,3] N. Wex,[2]
S. Osłowski,[1,2] B. W. Stappers,[4] C. G. Bassa,[5] R. N. Caballero,[2] D. J. Champion,[2]
I. Cognard,[6,7] G. Desvignes,[2] E. Graikou,[2] L. Guillemot,[6,7] G. H. Janssen,[5] A. Jessner,[2]
C. Jordan,[4] R. Karuppusamy,[2] M. Kramer,[2] K. Lazaridis,[2] P. Lazarus,[2] A. G. Lyne,[4]
J. W. McKee,[4] D. Perrodin,[8] A. Possenti[8] and C. Tiburzi[1,2]

[1]*Fakultät für Physik, Universität Bielefeld, Postfach 100131, D-33501 Bielefeld, Germany*
[2]*Max-Planck-Institut für Radioastronomie, Auf dem Hügel 69, D-53121 Bonn, Germany*
[3]*Argelander-Institut für Astronomie, Universität Bonn, Auf dem Hügel 71, D-53121 Bonn, Germany*
[4]*Jodrell Bank Centre for Astrophysics, School of Physics and Astronomy, The University of Manchester, Manchester M13 9PL, UK*
[5]*ASTRON, The Netherlands Institute for Radio Astronomy, Postbus 2, NL-7900 AA Dwingeloo, the Netherlands*
[6]*Laboratoire de Physique et Chimie de l'Environnement, CNRS, 3A Avenue de la Recherche Scientifique, F-45071 Orléans Cedex 2, France*
[7]*Station de radioastronomie de Nançay, Observatoire de Paris, CNRS/INSU, Université d'Orléans, F-18330 Nançay, France*
[8]*INAF – Osservatorio Astronomico di Cagliari, Via della Scienza 5, I-09047 Selargius (CA), Italy*

## ABSTRACT

Timing results for the black-widow pulsar J2051−0827 are presented, using a 21 year data set from four European Pulsar Timing Array telescopes and the Parkes radio telescope. This data set, which is the longest published to date for a black-widow system, allows for an improved analysis that addresses previously unknown biases. While secular variations, as identified in previous analyses, are recovered, short-term variations are detected for the first time. Concurrently, a significant decrease of $\sim 2.5 \times 10^{-3}$ cm$^{-3}$ pc in the dispersion measure associated with PSR J2051−0827 is measured for the first time and improvements are also made to estimates of the proper motion. Finally, PSR J2051−0827 is shown to have entered a relatively stable state suggesting the possibility of its eventual inclusion in pulsar timing arrays.

**Key words:** binaries: close – binaries: eclipsing – pulsars: general – pulsars: individual: PSR J2051−0827.

## 1 INTRODUCTION

Of the $\sim 2600$ pulsars known today, roughly 10 per cent appear to have rotation periods of the order of a few milliseconds and are known as millisecond pulsars (MSPs). Within the MSP population, there exist a variety of configurations; however, most MSPs are found in binary systems. Among these, about 10 per cent are in tight, eclipsing binaries. Such systems are further classified into the black-widow systems, with very light companions of mass ($\dot{m}_c \lesssim 0.05$ M$_\odot$) and redback systems, with heavier companions ($0.1$ M$_\odot$ $\lesssim \dot{m}_c \lesssim 0.5$ M$_\odot$; Chen et al. 2013; Roberts 2013). PSR J2051−0827 is the second black-widow system that was discovered (Stappers, Bessell & Bailes 1996). Its companion is expected to be a $\sim 0.02$–$0.06$ M$_\odot$ star, whose exact nature is yet to be determined (see discussions in Stappers et al. 2001; Lazaridis et al. 2011).

Pulsar timing relies on making highly precise measurements of the time at which the radio beam from a rotating pulsar crosses a radio telescope. These measured times are then compared to a theoretical prediction of these crossing events to derive various properties of the pulsar. A more extensive discussion on pulsar timing and the benefits of MSPs for pulsar timing can be found in Lorimer & Kramer (2005) and other reviews of pulsar timing.

MSPs are particularly well suited for this because of their inherent stability and short rotation periods. Even though the pulsars in black-widow systems are MSPs, they are typically excluded from high-precision pulsar timing experiments since several of them have been observed to display variability in their orbital parameters, in particular the orbital period. This variability may be due to many reasons like the interaction of the pulsar with the companion, the presence of excess gas around the companion's orbit or the companion's mass-loss.

However, only a limited number of studies so far have tried to identify if the variability of such pulsars can be modelled by

★ E-mail: golam.shaifullah@gmail.com

introducing new parameters into the pre-existing timing models or by defining new timing models for such systems. Given the recent increase in the number of MSPs detected, in large part from surveys of *Fermi*-LAT sources (Abdo et al. 2013), and the rapid growth in the sensitivity and bandwidth (BW) of modern digital receiver systems for pulsar timing making it possible to detect variations in much greater detail, it is pertinent to address this long-standing question.

PSR J2051−0827 has been continuously timed since its discovery in 1995 (Stappers et al. 1996) and therefore the data set presented in the following analysis represents the longest timing baseline currently published for eclipsing black-widow systems. Given this long time baseline and other favourable properties discussed in the following sections, this data set offers an ideal opportunity to attempt such an exercise.

Previous pulsar timing analyses of PSR J2051−0827 have shown that the orbital period, $P_b$, and projected semi-major axis, $x$, undergo secular variations (Stappers et al. 1998; Doroshenko et al. 2001; Lazaridis et al. 2011). These variations are possibly linked to the variations of the gravitational quadrupole (GQ) moment of the companion and induced by variations of the mass quadrupole of the companion as its oblateness varies due to rotational effects (Lazaridis et al. 2011). These variations may arise due to a differential rotation of the outer layers of the companion (Applegate & Shaham 1994) or due to variations in the activity of the magnetic field of the companion as in the Lanza & Rodonò (2001) model. Similar variations have been measured for a few other pulsars in BW systems like PSR J1959+2048 (PSR B1957+20; Fruchter, Stinebring & Taylor 1988), PSRs J0024−7204J and J0024−7204O (47 Tuc J and O; Freire et al. 2003), PSR J1807−2459A (NGC 6544A; Lynch et al. 2012) and PSR J1731−1847 (Ng et al. 2014).

The binary system containing PSR J2051−0827 has also been recently detected in *Fermi*-LAT and *Chandra*/ACIS data (Wu et al. 2012). The $\gamma$-ray luminosity is $7.66 \times 10^{32}$ erg s$^{-1}$. The inferred spin-down power, $\dot{E}$, from radio observations is $\sim 5.49 \times 10^{33}$ erg s$^{-1}$. The $\gamma$-ray luminosity, therefore, represents $\sim 15$ per cent of the total spin-down power, which is consistent with other MSPs for which such a detection has been made. The $\gamma$-ray emission from the system appears to be well fitted by a model of emission in the 'outer gap accelerator', as discussed in Takata, Cheng & Taam (2012). Using the new ephemerides presented here, it may be possible to detect the orbital dependence of pulsed emission from PSR J2051−0827.

The X-ray luminosity is $1.01 \times 10^{30}$ erg s$^{-1}$ (Wu et al. 2012), and the data do not present any evidence for bursts, which suggests that the companion is stable and does not undergo sudden deformations. The flux values fit well for a model with emission from the intra-binary shock, the polar caps and synchrotron emission from the pulsar magnetosphere (Wu et al. 2012).

This work provides an update on the timing of PSR J2051−0827 and presents an improved analysis. Two complementary timing models for PSR J2051−0827 are provided, one capable of handling small eccentricities and another utilizing orbital-frequency derivatives (OFDs). A new method for measuring the variations in the orbital period, $\Delta P_b$, by measuring the change in the epoch of ascending node, $T_{asc}$, is also presented.

## 2 OBSERVATIONS AND DATA ANALYSIS

The bulk of the data set used for the timing analysis consists of pulse times of arrival (henceforth ToAs) derived from data from four European Pulsar Timing Array (EPTA) telescopes[1] and extends from 2003 to 2015. To extend the analysis and to test for consistency with previous analyses, ToAs [obtained from the Lazaridis et al. (2011) data set] from the EPTA telescopes, in the period 1995–2009, and the Parkes radio telescope, extending from 1995 to 1998, were added to the data set. Wherever possible, these ToAs were replaced with new ToAs derived from data processed as described later in this section.

As a result of the extended temporal coverage, data files (henceforth archives) from a number of pulsar data recording instruments or 'backends' are included in the data set. These include the Effelsberg-Berkeley Pulsar Processor (EBPP), the Berkeley-Orleans-Nançay (BON) instrument, the Digital Filter Bank (DFB) and the Pulsar Machine I (PuMa-I) backend, all described in Desvignes et al. (2016) as well as the Analogue Filter Bank (Shemar & Lyne 1996) at Jodrell Bank and, the new generation of pulsar timing backends, namely, PuMa-II at the WSRT (Karuppusamy, Stappers & van Straten 2008), PSRIX at Effelsberg (Lazarus et al. 2016), ROACH at Jodrell Bank (Bassa et al. 2016) and the Nançay Ultimate Pulsar Processing Instrument (NUPPI) at Nançay (Desvignes et al. 2011). The names of all the backends and their respective telescopes can be found in Table 1.

The archives from all the backends were first re-weighted by the square root of the signal-to-noise ratio (S/N) and then grouped into 5 min integrations using the psradd tool from the PSRCHIVE[2] suite (Hotan, van Straten & Manchester 2004; van Straten, Demorest & Oslowski 2012).

ToAs were generated via cross-correlations of the time-integrated, frequency-scrunched, total intensity profiles with noise-free analytical templates, constructed by fitting high-S/N pulse profiles with a set of von Mises functions using the paas tool of PSRCHIVE. These templates were manually aligned using pas. The pat tool from the same suite was used to generate ToAs, with the Fourier domain with Markov chain Monte Carlo algorithm (a re-implementation of Taylor 1992) and goodness-of-fit (GOF) flags were enabled for the ToAs, as advised by Verbiest et al. (2016). A summary of the data from the different backends and telescopes is provided in Table 1. Fig. 1 shows a plot of the timing residuals for the entire 21 year span, when the ToAs are fitted to the BTX model, as explained below.

Instrumental offsets between the various backends were corrected for by using 'JUMP' statements, which allow correct error propagation.

For the PSRIX backend (Lazarus et al. 2016) at the Effelsberg radio telescope, which has a total BW of 200 MHz at 21 cm wavelength and the archives with the highest S/N (up to $\sim 4000$, for a particular observation), archives were tested for frequency evolution of the pulse shapes. The data were split into 25 MHz channels and analytical templates were generated for each band, as explained above. These templates were manually compared using the paas tool. No significant differences were detected and the data were recombined into the full 200 MHz band. For the other backends, such an exercise is not possible since either the S/N is typically worse or the BW is too low to detect any obvious frequency

---

[1] These are the Effelsberg 100 m radio telescope, the Lovell radio telescope at Jodrell Bank, the Nançay radio telescope and the Westerbork Synthesis Radio Telescope (WSRT). A fifth telescope, the Sardinia Radio Telescope (SRT), has just entered its initial operational phase and therefore no data from the SRT are included here.

[2] Commit hash - 87357c2; psrchive.sourceforge.net

**Table 1.** Telescope and receiver-wise description of the data set, showing the bandwidth (BW), the centre frequency of observations ($f_c$), the number of ToAs retained after the selection process described in the text and the MJD ranges over which the ToAs exist. For the older backends (see the text), only ToAs were available. For the new backends, archives were processed as described in Section 2.

| Telescopes and receivers used for the data set | | | | |
|---|---|---|---|---|
| Telescope +Backend | BW (MHz) | $f_c$ (MHz) | No. of ToAs | MJD range |
| Effelsberg | 28 | 840 | 24 | 51772–53159 |
| +EBPP | 56 | 1410 | 690 | 50460–54791 |
| | 112 | 2639 | 35 | 51247–54690 |
| +PSRIX | 200 | 1360 | 120 | 55759–56494 |
| | 100 | 2640 | 116 | 55632–56779 |
| Lovell | 16 | 410 | 8 | 50157–50695 |
| +A/DFB | 16 | 610 | 42 | 50021–51452 |
| (see note below) | 16 | 1400 | 154 | 49989–54853 |
| +ROACH | 400 | 1532 | 844 | 55656–56729 |
| Nançay+BON | 128 | 1397 | 4502 | 53293–54888 |
| +NUPPI | 512 | 1484 | 2324 | 55817–56700 |
| WSRT+PuMa | 80 | 1380 | 20 | 54135–54372 |
| +PuMa-II | 80 | 345 | 1173 | 54490–56640 |
| | 160 | 1380 | 536 | 54520–56640 |
| Parkes | 128 | 1400 | 23 | 50116–50343 |
| +FPTM | 128 | 1700 | 31 | 50116–50343 |

*Note.* The figures for bandwidth (BW) and centre frequency ($f_c$) for the Jodrell Bank A/DFB and Parkes data are indicative only since the observations were made with various configurations. Details for these can be found in Stappers et al. (1998). Similar details for the other telescopes can be found in Desvignes et al. (2016), Bassa et al. (2016) or other specific references listed in Section 2.
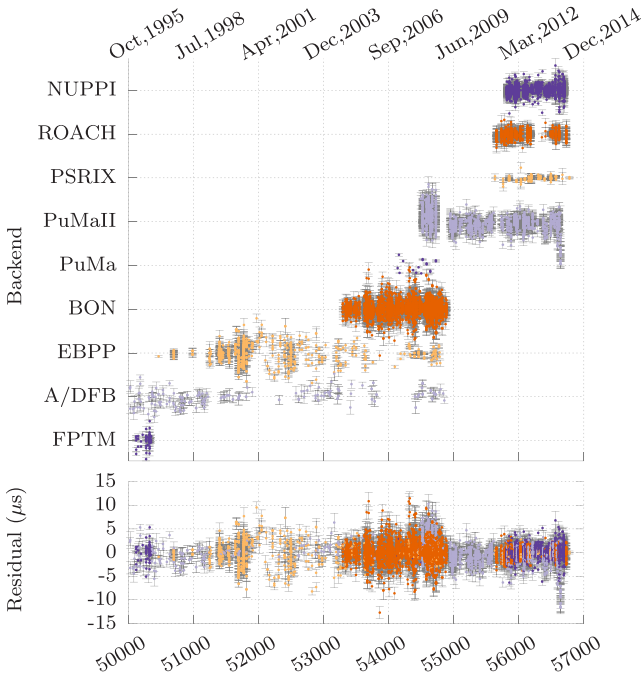


**Figure 1.** Plot of ToAs as a function of MJD. The bottom plot shows the timing residual from fitting the ToAs to the BTX model (see Section 2). The top plot shows the same but with manually introduced offsets to show the ToAs grouped by their respective backends. See Table 1 for the details of the backends.

evolution in the pulse profile. ToAs were also generated by using templates from different backends to test for pulse shape differences between backends. The timing analysis was then carried out using the TEMPO2[3] package (Hobbs, Edwards & Manchester 2006). Observations which were linked to ToAs with unexplained residual offsets $\gtrsim 3\sigma$ were manually investigated. In some cases, manual radio-frequency interference excision was sufficient to remove the offset. A few ToAs were found to be linked to observations with previously determined time offsets, which were corrected for using the TEMPO2 TIME keyword in the relevant sections of the ToA files. In a few cases, ToAs were found to have offsets which could not be corrected by either of the two methods. In most cases, these ToAs were found to have poor GOF values ($\geq 2$) from the template matching and therefore, removed from the data set. These ToAs are being investigated further to determine their possible association with micro-eclipses of the kind demonstrated by Archibald et al. (2009). However, their exclusion does not affect any of the conclusions in this analysis.

Similar to previous analyses, ToAs corresponding to orbital phases 0.2–0.35 [determined using the ephemeris presented in Lazaridis et al. (2011)] were removed as the eclipse region lies within that range. When carrying out a weighted fit, ToAs with large uncertainties contribute only weakly to the timing solutions and can often be discarded without greatly affecting the results. For MJD ranges with dense temporal sampling, a cut-off of 20 µs was applied. For the MJD range ∼52000–53000, where the number of ToAs was very low even before a cut-off was applied, only ToAs with uncertainties greater than 60 µs were removed.

After the ToA selection procedure described above, the ToAs were split into ∼1095 d (or 3 year) long 'aeons' with an overlap of 365 d between successive aeons. For each aeon, the ToAs were fitted to the ELL1 (Lange et al. 2001) timing model, while keeping the dispersion measure (DM) fixed and setting the reference epoch to the centre of the aeon. The timing solutions were derived using the NASA-JPL DE421 planetary ephemeris (Folkner, Williams & Boggs 2009). The reference clock used was the Terrestrial Time standard derived from the 'Temps Atomique International' time standard, denoted by TT(TAI), and the final ToAs were corrected according to the Bureau International des Poids et Mesures standards (see e.g. Hobbs et al. 2006, and references therein). The default TEMPO2 assumptions for the solar-wind model were retained for this analysis.

When using data from multiple instruments, it is necessary to correct the possible misestimation of the uncertainty of the ToAs in order to correct for the relative weighting of data from different backends. TEMPO2 error scaling factors (or T2EFACs) were calculated for each backend by applying the timing model derived in the previous step (without re-fitting) and then taking the square root of the reduced $\chi^2$. The corresponding ToA uncertainties were then multiplied by these T2EFAC values.

For the ELL1 model, the $\sigma/\sqrt{N}$ statistic, where $\sigma$ is the timing residual and $N$ is the number of ToAs, is used to select the aeon with the most information. From Table 2, this is identified as the epoch starting at MJD 55121. The timing parameters for this aeon are presented in Table 4, and a comparison with published literature is provided in Table 3.

As is obvious from the preceding discussions, the ELL1 model requires updating at regular intervals or aeons. This is a consequence of the orbital variability of this system, as discussed in Section 3.3.

---

[3] version - 2013.9.1 with updated clock files; http://www.atnf.csiro.au/research/pulsar/tempo2

**Table 2.** Properties of the ToA sets for each individual aeon (∼1095 MJD period), determined using the respective ELL1 models. Note that the reduced $\chi^2$ values shown below are derived after applying error scaling or EFACs as described in Section 2.

| MJD range | Aeon-wise properties of data set | | |
| --- | --- | --- | --- |
| | Weighted rms timing residual ($\mu$s) | Reduced $\chi^2$ value | Number of ToAs |
| 49989–51062 | 8.9 | 1.0 | 143 |
| 50724–51812 | 13.2 | 1.0 | 331 |
| 51451–52538 | 14.2 | 0.9 | 195 |
| 52213–53258 | 19.3 | 1.0 | 146 |
| 52927–54004 | 9.2 | 1.5 | 1037 |
| 53643–54733 | 9.5 | 1.0 | 2518 |
| 54372–55444 | 10.8 | 1.4 | 1959 |
| 55121–56189 | 5.0 | 1.1 | 1679 |
| 55836–56880 | 6.2 | 0.9 | 2110 |

Therefore, the BTX model was used to construct a single timing model encompassing the entire 21 year period.

The BTX model is a re-implementation of the BT model (Blandford & Teukolsky 1976) and incorporates higher order derivatives of the orbital frequency. This model is completely phenomenological and thus has no predictive power. The model also demands judicious usage since the highest order OFDs can easily introduce correlations with proper motion components, DM variations and instrumental offsets, particularly in this highly heterogeneous data set. Eccentricity measurements from the ELL1 models show large variability along with low measurement significance, indicating that these measurements are probably unreliable. Hence, the BTX model was created with eccentricity set to zero.

To limit the number of OFDs employed in the BTX model, the reduced $\chi^2$ was used as the primary selection criterion. The reduced $\chi^2$ remains well above 10 until the 17th OFD is introduced. Subsequent OFDs do not affect the reduced $\chi^2$ and are not determined with any significance by TEMPO2. Amongst the timing models with 13 or more OFDs, the Akaike Information Criterion (Akaike 1974) also favours the model with 17 OFDs. The BTX timing parameters with 17 OFDs for PSR J2051−0827 are presented in Table 4.

The timing models and ToAs are available under 'additional online material' at the EPTA web page, accessible via http://www.epta.eu.org/aom.html.

# 3 TIMING RESULTS

## 3.1 Proper motion

PSR J2051−0827 has a low ecliptic latitude of ∼8°.85. Typically for such low latitudes, the determination of position is relatively poor (Lorimer & Kramer 2005). Therefore, the resulting measurement of proper motion in declination or ecliptic latitude (depending on the coordinate system used) is imprecise. This is evident in the published values of proper motion in declination, $\mu_\delta$, presented in Table 3.

To improve the measurement and utilize the entire 21 year span of the data set, the measured values of right ascension (RA) and declination (Dec.) for each aeon were fitted with a linear function to obtain a mean proper motion. This results in a significant measurement of $\mu_\alpha$ and $\mu_\delta$, as shown in Fig. 2 and Table 3. The fitted values of $\mu_\alpha$ and $\mu_\delta$ are inserted into the ELL1 models for each aeon and those models are re-fitted for the other parameters.

Using an estimated distance of ≃1040 pc (from the NE2001 model of free-electron distribution in the Galaxy; Cordes & Lazio 2003) and a total proper motion $\mu_t = \sqrt{\mu_\alpha^2 + \mu_\delta^2} = 6.1 \pm 0.1$ mas yr$^{-1}$, a 2D transverse velocity of $v_t = 30 \pm 9$ km s$^{-1}$ was calculated. This assumes an uncertainty of 30 per cent[4] in the DM-derived distance mentioned above. The measurement is in agreement with the value of $30 \pm 20$ km s$^{-1}$ measured by Stappers et al. (1998) and represents a twofold increase in precision, even though the uncertainty of the DM-derived distance is assumed to be much greater. It should be noted that this is significantly lower than the average value of $93 \pm 13$ km s$^{-1}$ reported in Desvignes et al. (2016) for the transverse velocities of binary MSPs. However, it agrees well with the value of $56 \pm 3$ km s$^{-1}$ reported for the binary MSPs with distance measurements from parallaxes.

The proper motion values obtained from the BTX model appear to be inconsistent with those obtained from fitting to position measurements for every aeon using the respective ELL1 models. This is because the proper motion terms and the OFDs are strongly covariant and therefore the uncertainties in the values obtained from the BTX model are heavily underestimated, reinforcing the need for cautious usage of this model.

## 3.2 DM variations

Since the DM is a measure of the density of the ionized interstellar medium (IISM) along the line of sight to the pulsar, both the motion of the pulsar and the dynamical evolution of the IISM affect this value. While it is possible to obtain the DM from timing, 'JUMPS' or instrumental offsets introduced to align the ToAs from the different backends are fully covariant with the DM and prevent an accurate measurement directly from the data set presented above. Therefore, a DM value of 20.7299(17) cm$^{-3}$ pc is adopted from the LOFAR measurements of Kondratiev et al. (2016).

When simultaneous dual (or multi-) frequency observations are available, it is, however, possible to accurately estimate the *variation* in the DM. The WSRT PuMa-II backend provides observations centred at 345 and 1380 MHz, with a cadence of roughly three weeks. Observations between the two frequencies are sequential, which are separated by, at most, a few days and available for the MJD range ∼54600–56800. Since low-frequency observations are more sensitive to the DM variations, these are utilized to measure them instead of the two frequency-band observations of the PSRIX backend.

To measure DM variations, the PuMa-II ToAs were fitted for DM using the ELL1 model presented in Table 4. The ToAs were then split into 100 d long intervals, to ensure that enough data were available for a reliable estimate. Each 100 d interval was then re-fitted for the DM, $P_b$ and $T_0$. The fit for $P_b$ is necessary to ensure that orbital-phase-dependent effects do not contaminate the DM measurement, since the observations at 345 and 1380 MHz do not necessarily coincide in orbital phase.

This leads to a significant detection of a DM trend after MJD 54600, which is plotted in Fig. 3. A quadratic fit returns a reduced $\chi^2$ of 3.5 while a linear fit performs not much worse, with a reduced $\chi^2$ of 6. The linear trend appears to show a weakly sinusoidal residual, with a 'best-fitting' period of ∼940 d but this residual

---

[4] See Desvignes et al. (2016) for a discussion on the possible underestimation of uncertainties of the DM-derived distances.

**Table 3.** Comparison of selected parameters of the black-widow pulsar system J2051−0827 with published values. $\mu_\alpha$ and $\mu_\delta$ values for the ELL1 model are obtained from a weighted fit to the position measured at successive aeons. The epoch of DM determination need not correspond with the epoch of the timing model since the DM values for the ELL1 models are fixed from Kondratiev et al. (2016), as explained in Section 3.2. Similarly, the DM value used in the Lazaridis et al. (2011) analysis is taken from Stappers et al. (1998).

| Parameter | Doroshenko et al. (2001) | Lazaridis et al. (2011) | ELL1 model (Best fit) |
|---|---|---|---|
| MJD range of timing model fit | 49573–51908 | 53293–54888 | 55121.8–56189.9 |
| Proper motion in RA, $\mu_\alpha$ (mas yr$^{-1}$) | 5.3(10) | 6.6(2) | 5.63(4) |
| Proper motion in Dec., $\mu_\delta$ (mas yr$^{-1}$) | 0.3(30) | 3.2(7) | 2.34(28) |
| Dispersion measure, DM (pc cm$^{-3}$) | 20.7449(4) | 20.7458(2) | 20.7299(17) |
| Epoch of DM measurement (MJD) | 51000.0 | 49530.0 | 56387.8 |
| Eccentricity, $e$ | $<9.6 \times 10^{-5}$ | $6(1) \times 10^{-5}$ | $5.1(8) \times 10^{-5}$ |
| Reduced $\chi^2$ (with scaled uncertainties) | – | 1 | 1.1 |
| Number of ToAs | 584 | 3126 | 1679 |
| Solar system ephemeris model | DE200 | DE405 | DE421 |
| Timing software package | TIMAPR/TEMPO | TEMPO2 | TEMPO2 |

becomes insignificant with the quadratic model and therefore, no higher order model was considered.

While it is quite possible that such variations may be present before MJD 54600, the lack of sensitivity due to sparse and inhomogeneous multi-frequency observations leads to typical DM measurement uncertainties of $\sim 1 \times 10^{-3}$ to about $\sim 3 \times 10^{-4}$ cm$^{-3}$ pc. These uncertainties, which may well be severely underestimated, prevent any firm conclusion on the DM evolution. Furthermore, because no combination of two observing systems at different frequencies is continuously present before MJD 54600, any effort to measure DM variations in that MJD range is necessarily corrupted by the arbitrary phase offsets used to align the data from different instruments. The WSRT data which provide continuous data at two frequencies after MJD 54600 provide a DM precision of $\lesssim 3 \times 10^{-4}$ cm$^{-3}$ pc over 100 d intervals, allowing accurate DM modelling over that period.

Traditionally, wherever a DM trend is observed, it is corrected for by introducing DM derivatives.[5] Given the large uncertainties in the earliest eras and to prevent overfitting or accidentally introducing excess white noise in the timing, only those ToAs belonging to the period over which a clear DM trend is measured are corrected for the DM trend modelled by the quadratic fit shown in Fig. 3. This is implemented by introducing a TEMPO2 DM offset flag (-dmo) for the ToAs lying in the MJD range 54600–56800.

### 3.3 Secular variations

Following Lazaridis et al. (2011), variations in the binary period ($P_b$) and the projected semi-major axis ($x$) were measured by splitting the ToAs into 'eras' of approximately 365 d. The results of reproducing and extending the Lazaridis analysis[6] are presented in Fig. 4.

The simultaneous fitting of $P_b$, $x$ and $T_{\rm asc}$, as in Lazaridis et al. (2011), is undesirable since $P_b$ and $T_{\rm asc}$ are fully covariant parameters. In practice, wherever good orbital-phase coverage ($\geq 60$ per cent) is available, the measurement of $T_{\rm asc}$ is far more accurate and reliable since it measures the orbital phase and requires less information for its calculation than $P_b$. Due to the high

---

[5] For detailed reviews on modern DM correction methods, see Verbiest et al. (2016), Demorest et al. (2013) or Lentati et al. (2015).

[6] In the Lazaridis et al. (2011) analysis, timing models are first derived for the largest MJD range over which a TEMPO2 fit converges, which are analogous to 'aeons' in the present work. Then, the variations in $P_b$ and $x$ are measured by fitting for $P_b$, $x$ and $T_{\rm asc}$ simultaneously for 300 d periods with an overlap of 30 d.

cadence and long durations of the Nançay, Jodrell Bank and WSRT observations and full orbital observations at Effelsberg, especially in the latest years, it is possible to carry out such a measurement with much greater precision than was previously attempted.

By keeping $P_b$ constant for all eras, and fitting for $T_{\rm asc}$, $x$ and the Laplace–Lagrange parameters, $\eta = e \cdot \sin\omega$ and $\kappa = e \cdot \cos\omega$ simultaneously, the change in $T_{\rm asc}$ is measured. The change in $P_b$ measured at time $t_1$, $\Delta P_{b,t_1}$, is then calculated using the equation

$$\Delta P_{b,t_1} = \frac{T_{\rm asc,t_1} - T_{\rm asc,t_0}}{t_1 - t_0} \times P_{b,\rm ref}, \qquad (1)$$

where $T_{\rm asc,t_0}$ and $T_{\rm asc,t_1}$ are the values of $T_{\rm asc}$ at two neighbouring eras $t_0$ and $t_1$. $P_{b,\rm ref}$ is a constant $P_b$ value chosen from the $P_b$ values for each epoch, such that the measured $\Delta T_{\rm asc}$ values do not show any obvious slope. The resulting $\Delta P_b$ variations and the $\Delta T_{\rm asc}$ from which they are derived are plotted in Fig. 5, along with the simultaneous $\Delta x$ measurements. The measured values for all three parameters are overplotted with the interpolation of the change in $\Delta T_{\rm asc}$ as obtained from the BTX model (see e.g. Ng et al. 2014). The excellent agreement serves to further confirm the applicability of the BTX model.

Comparing the $P_b$ variations derived from the $T_{\rm asc}$ variations in Fig. 5 and those in Fig. 4, derived from the Lazaridis et al. (2011) method, it is apparent that fitting for all three parameters introduces a 'smoothing' effect. This is likely due to the covariance of $P_b$ and $T_{\rm asc}$ and thus demonstrates the importance of estimating $\Delta P_b$ from fitting for $T_{\rm asc}$ and $x$ simultaneously. It should be noted that for all the eras that were analysed, $P_b$ and $T_{\rm asc}$ were found to be either strongly correlated or anti-correlated ($|{\rm corr.}| \geq 0.9$), with a somewhat alternating behaviour, while the $P_b$ and $x$ are always weakly correlated ($|{\rm corr.}| \leq 0.3$). Finally, $T_{\rm asc}$ and $x$ are always very weakly correlated ($|{\rm corr.}| \ll 0.3$).

As can be seen from Fig. 5, the new analysis is in qualitative agreement with the measurements presented in Lazaridis et al. (2011) and the system appears to have entered a 'quieter' phase. For brevity, only a summary of the maximum possible contribution to the secular variations from the various possible sources is presented in Table 5. For a full discussion of these, see Lazaridis et al. (2011).

Variations in the orbital period can be attributed to contributions due to gravitational-wave emission ($\dot{P}_b^{\rm GW}$), changing Doppler shift ($\dot{P}_b^{\rm D}$), mass-loss from the companion ($\dot{P}_b^{\rm m}$), tidal interactions between the companion and the pulsar ($\dot{P}_b^{\rm T}$) and variations of the GQ

**Table 4.** Timing parameters for PSR J2051−0827 for the ELL1 (implemented via the TEMPO2 hybrid model T2) and the BTX models. The values of derived parameters are italicized while parameters that should be necessarily excluded from the respective timing models are marked as N/A. Note that the DM values presented here are obtained from Kondratiev et al. (2016). For brevity, this table uses the following abbreviations: FB0 indicates orbital frequency and higher numbers the resp. derivative, NToA denotes the number of ToAs, rms $t_{resid}$ denotes the rms timing residual and Red. $\chi^2$ is the reduced $\chi^2$ value for the weighted TEMPO2 fit. $\tau_{char}$ is the characteristic age associated with the pulsar and $B_{surf}$ is the estimated surface magnetic field strength. The TT(TAI) clock correction procedure and the DE421 solar system ephemerides were used for both the models. The units are in TCB (see Hobbs et al. 2006, for details). The figures in parentheses are the nominal $1\sigma$ TEMPO2 uncertainties in the least-significant digits quoted. The coordinates refer to J2000.

| Pulsar name | PSR J2051−0827 | |
|---|---|---|
| Binary model | T2 | BTX |
| MJD range | 55121.8–56189.9 | 49989.9–56779.3 |
| NToA | 1679 | 11 391 |
| rms $t_{resid}$ ($\mu s$) | 5.0 | 5.2 |
| Red. $\chi^2$ | 1.1 | 4.2 |
| RA, $\alpha$ | 20:51:07.519 768(18) | 20:51:07.519 763(8) |
| Dec., $\delta$ | −08:27:37.7497(8) | −08:27:37.7505(4) |
| Ec. Long., $\lambda$ | 312.835 726 88(8) | 312.835 727 10(2) |
| Ec. Lat., $\beta$ | 8.846 3418(5) | 8.846 342 30(9) |
| $\mu_\alpha$ (mas yr$^{-1}$) | 5.63(4) | 5.57(4) |
| $\mu_\delta$ (mas yr$^{-1}$) | 2.34(28) | 3.60(10) |
| $\mu_\lambda$ (mas yr$^{-1}$) | 7.2(3) | 6.34(1) |
| $\mu_\beta$ (mas yr$^{-1}$) | 4.6(23) | 1.9(1) |
| $\nu$ (s$^{-1}$) | 221.796 283 653 017(5) | 221.796 283 653 0492(10) |
| $\dot{\nu}$ (s$^{-2}$) | −6.264(3)× 10$^{-16}$ | −6.265 32(6)× 10$^{-16}$ |
| *P* (ms) | *4.508 641 820 006 43(8)* | *4.508 641 820 0061(5)* |
| $\dot{P}$ | *1.2732(4)× 10$^{-20}$* | *1.273 74(3)× 10$^{-20}$* |
| DM (cm$^{-3}$ pc) | 20.7299(17) | 20.7299(17) |
| *x* (lt-s) | 0.045 0720(3) | 0.045 070 74(20) |
| $\dot{x}$ | 1.3(148)× 10$^{-16}$ | 9.6(12)× 10$^{-15}$ |
| $P_b$ (d) | 0.099 110 254 90(4) | N/A |
| $\dot{P}_b$ | −5.9(3)× 10$^{-12}$ | N/A |
| FB0(Hz) | N/A | 1.167 797 9406(7)× 10$^{-4}$ |
| FB1($s^{-2}$) | N/A | 8.2(4)× 10$^{-20}$ |
| FB2($s^{-3}$) | N/A | −7.4(3)× 10$^{-27}$ |
| FB3($s^{-4}$) | N/A | −6.3(16)× 10$^{-35}$ |
| FB4($s^{-5}$) | N/A | 3.9(8)× 10$^{-42}$ |
| FB5($s^{-6}$) | N/A | 1.8(7)× 10$^{-49}$ |
| FB6($s^{-7}$) | N/A | 6.5(24)× 10$^{-57}$ |
| FB7($s^{-8}$) | N/A | −5.8(23)× 10$^{-64}$ |
| FB8($s^{-9}$) | N/A | −4.0(8)× 10$^{-71}$ |
| FB9($s^{-10}$) | N/A | 1.6(7)× 10$^{-78}$ |
| FB10($s^{-11}$) | N/A | 1.4(3)× 10$^{-85}$ |
| FB11($s^{-12}$) | N/A | −3.2(18)× 10$^{-93}$ |
| FB12($s^{-13}$) | N/A | −3.7(8)× 10$^{-100}$ |
| FB13($s^{-14}$) | N/A | 3.0(30)× 10$^{-108}$ |
| FB14($s^{-15}$) | N/A | 7.3(19)× 10$^{-115}$ |
| FB15($s^{-16}$) | N/A | 5.2(20)× 10$^{-123}$ |
| FB16($s^{-17}$) | N/A | −7.9(25)× 10$^{-130}$ |
| FB17($s^{-18}$) | N/A | −1.8(5)× 10$^{-137}$ |
| Ref. epoch (MJD) | 55655 | 55655 |
| $\omega$ (deg) | *36(10)* | 0 |
| EPS1 | 3.0(10)× 10$^{-5}$ | N/A |
| EPS2 | 4.1(9)× 10$^{-5}$ | N/A |
| *e* | *5.1(8)× 10$^{-5}$* | 0 |
| TASC (MJD) | 54091.0343079(8) | *54091.03434936(14)* |
| T0 (MJD) | *54091.044(2)* | 54091.03434936(14) |
| $\log_{10}\tau_{char}$ (yr) | *9.75* | *9.75* |
| $\log_{10}B_{surf}$ (G) | *8.38* | *8.38* |
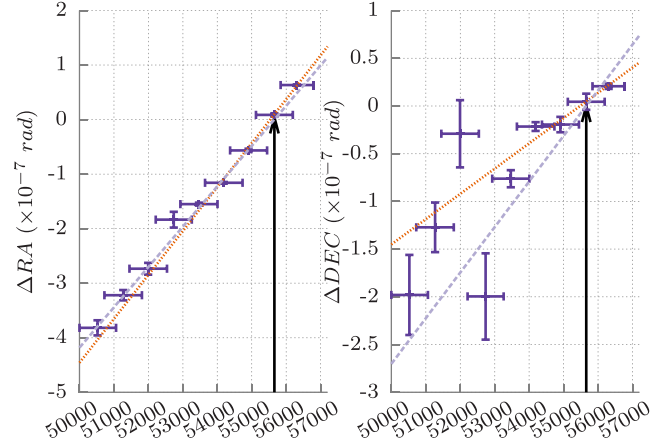


**Figure 2.** Measured values of RA (left) and Dec. (right) of PSR J2051−0827 for each aeon (purple +) and linear fits to those. Black arrows indicate the values at the reference epoch at which the two timing models of Table 4 are defined, MJD 55655. The fit to the position at the median MJD of each aeon (the finely dotted orange line) returns $\mu_\alpha = 5.63 \pm 0.10$ mas yr$^{-1}$ and $\mu_\delta = 2.34 \pm 0.28$ mas yr$^{-1}$ while the dashed lilac line represents the values obtained from the BTX model, shown in Table 4.
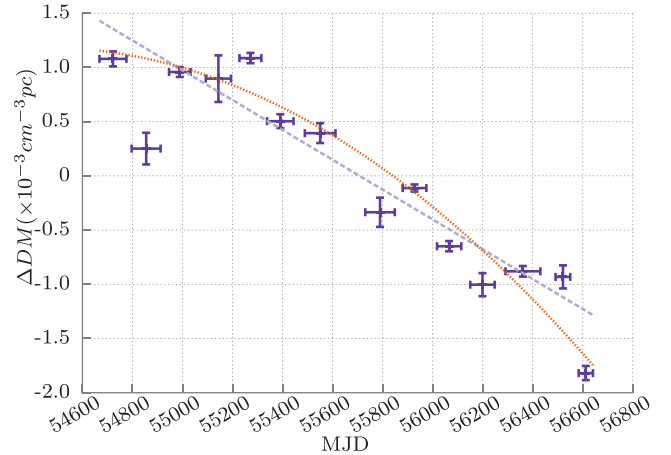


**Figure 3.** DM variation from consecutive 327 and 1380 MHz observations with the WSRT which extend over the period 54600–56800. A linear fit (lilac, dashed) and a quadratic fit (orange, finely dotted) are also shown.

moment of the companion star ($\dot{P}_b^Q$) (see for instance, Lorimer & Kramer 2005):[7]

$$\dot{P}_b^{obs} = \dot{P}_b^{GW} + \dot{P}_b^{\dot{D}} + \dot{P}_b^{\dot{m}} + \dot{P}_b^T + \dot{P}_b^Q. \qquad (2)$$

Similarly, the secular variations in the projected semi-major axis can be split into contributions due to radiation of gravitational waves ($\dot{x}^{GW}$), the proper motion of the pulsar ($\dot{x}^{PM}$), varying aberrations ($\frac{d\epsilon_A}{dt}$), changing Doppler shift ($\dot{x}^{\dot{D}}$), mass-loss in the binary system ($\dot{x}^{\dot{m}}$), variations of the GQ moment of the companion star ($\dot{x}^Q$), spin-orbit coupling of the companion ($\dot{x}^{SO}$) and a second, or planetary, companion ($\dot{x}^p$),

$$\dot{x}^{obs} = \dot{x}^{GW} + \dot{x}^{PM} + \frac{d\epsilon_A}{dt} + \dot{x}^{\dot{D}} + \dot{x}^{\dot{m}} + \dot{x}^Q + \dot{x}^{SO} + \dot{x}^p. \qquad (3)$$

[7] The sign on the $\dot{P}_b^{\dot{D}}$ and $\dot{x}^{\dot{D}}$ terms is made positive for the sake of uniformity here.
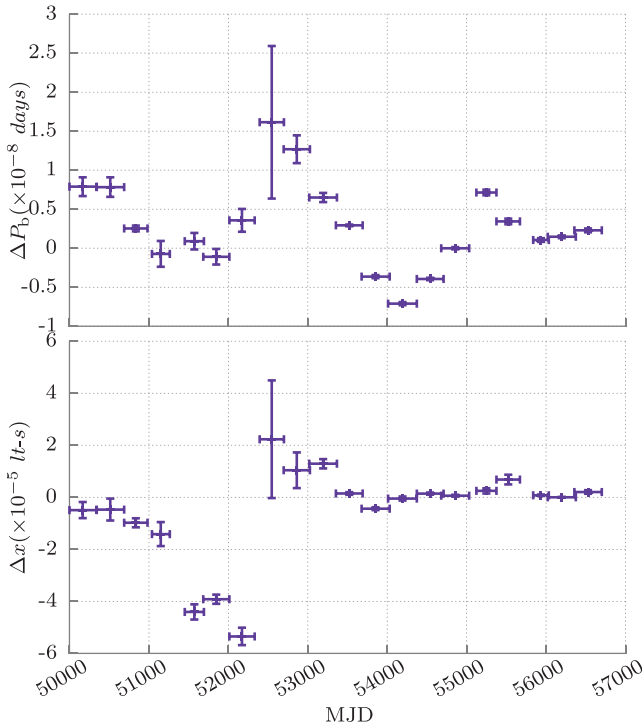
**Figure 4.** Change in $P_b$ and $x$ measured by fitting for $P_b$, $x$ and $T_{asc}$ for eras of length 365 d with an overlap of 30 d, where possible.

For the observed 21 year baseline, the maximum $\dot{P}_b$ is $\sim 1.41 \times 10^{-11}$ and the minimum is $\sim -2.03 \times 10^{-11}$. From Table 5, it is evident that the first four terms of equation (2) cannot drive the observed $\Delta P_b$ variations independently. Therefore, the hypothesis of Lazaridis et al. (2011) that the mass quadrupole variations in the companion are the most likely drivers of the observed $\Delta P_b$ variations is recovered.

Similarly, from Fig. 5, the variation of the projected semi-major axis shows a strong 'feature' in the MJD range $\sim 51000$–53000, which is not present in the remaining data. Since the correlation between $x$ and $T_{asc}$ or $x$ and $P_b$ is very weak, the differences between the bottom panels of Figs 4 and 5 are marginal, although the uncertainties in the second case are typically smaller for the 365 d epochs.

As in the case of the $\Delta P_b$ variations, the terms of equation (3) for which values are presented in Table 5 are not likely to be independent drivers of the variations in $\Delta x$. This implies that the Lazaridis et al. (2011) conjecture that the classical spin-orbit coupling term combined with the GQ term is the most likely driver for the $\Delta x$ variations is also recovered.

In addition to recovering the long-term fluctuations, the derivation of $\Delta P_b$ from $\Delta T_{asc}$ reveals small-scale variations, as indicated with black arrows in Fig. 6. These points lie $\gtrsim 4\sigma$ away from their local means and do have corresponding values with negative offsets. Given the results from Wu et al. (2012) presented in Section 1, it remains unclear what processes could lead to such deviations.

It is evident that continued multi-band monitoring of PSR J2051−0827 is necessary to reveal the origin of these sudden, sharp increases in the orbital period. If these changes are a result of activity of the companion, a greater understanding of the origin of these changes might help to understand the processes which drive state changes in the 'transitioning' MSP systems, i.e. binaries where the

MSP alternates between accreting and radio-pulsar states (see e.g. Stappers et al. 2014).

Given the high cadence and regular sampling in the later aeons, a test for the presence of a second companion, possibly of planetary dimensions, is carried out as well. This involves testing for the presence of higher order derivatives of pulse frequency in the timing solution (Joshi & Rasio 1997). The extrema of the second- and third-order frequency derivatives from TEMPO2 fits to the aeons are $-4.1(8) \times 10^{-24}$ s$^{-3}$ $\leqslant f^{(2)}_{max} \leqslant 3.0(19) \times 10^{-24}$ s$^{-3}$ and $1.1(6) \times 10^{-30}$ s$^{-4}$ $\leqslant f^{(3)}_{max} \leqslant 2.1(9) \times 10^{-30}$ s$^{-4}$. Since these values are at best marginally significant and in the absence of any supporting evidence from optical observations, the hypothesis of a second companion to PSR J2051−0827 remains unjustified.

## 4 HIGH-PRECISION TIMING PROSPECTS

Due to the complicated and somewhat arbitrary orbital variability that some pulsars in BW systems have been shown to exhibit (e.g. Nice, Arzoumanian & Thorsett 2000; Freire et al. 2003; Lynch et al. 2012; Ng et al. 2014), these sources have been traditionally left out of high-precision pulsar timing campaigns. With the recent increase in the number of BW systems discovered among the *Fermi* sources (Abdo et al. 2013), it will soon be possible to quantify these instabilities for a larger sample. As a counter-example to the current practice, the pulsar of the BW system J0610−2100 has recently been added to the list of sources for the EPTA (Desvignes et al. 2016) and has, so far, provided stable timing.

Simulations for pulsars timed using the BTX model by Bochenek, Ransom & Demorest (2015) show that only a small percentage of the power from gravitational waves is likely to be absorbed into the higher order OFDs and again appear to favour the inclusion of such pulsars in PTAs. However, Bochenek et al. (2015) do not take into consideration variations of $x$, as identified for the BW system J2051−0827.

The timing analysis presented here demonstrates the practical usability of the BTX model for such systems. However, it should also be noted that the GOF for the BTX model is still rather low as some variations remain unaccounted for.

It is probably an opportune coincidence that the BW system J2051−0827 has entered a relatively stable phase, suggesting greater usability for a PTA. Even without addressing some of the ambiguities in the fundamental properties of this system, for both the ELL1 and BTX models, the present analysis shows that it is possible to obtain timing residuals of the order of $\sim 5.0$ $\mu$s, quite comparable to the timing precision of several sources already in the PTAs (Verbiest et al. 2016). In the intermediate- to high-S/N regime of gravitational-wave background observations, where the number of pulsars are more important than very high timing precision (Siemens et al. 2013), timing residuals of the order of 1 $\mu$s could be sufficient. With the advent of the new 'ultra-broad-band' backends (Karuppusamy, private communication) and rapid increases in sensitivity, this does not appear to be an unrealistic goal.

## 5 SUMMARY

A timing update on PSR J2051−0827 is presented, along with timing models for the BTX and ELL1 models of TEMPO2. An improved estimate of the mean proper motion is also made, giving a value of $30 \pm 9$ km s$^{-1}$. A significant decrease in the DM of $\sim 2.5 \times 10^{-3}$ cm$^{-3}$ pc is detected for the MJD range 54600–56800 and corrections are incorporated in the ToA file.
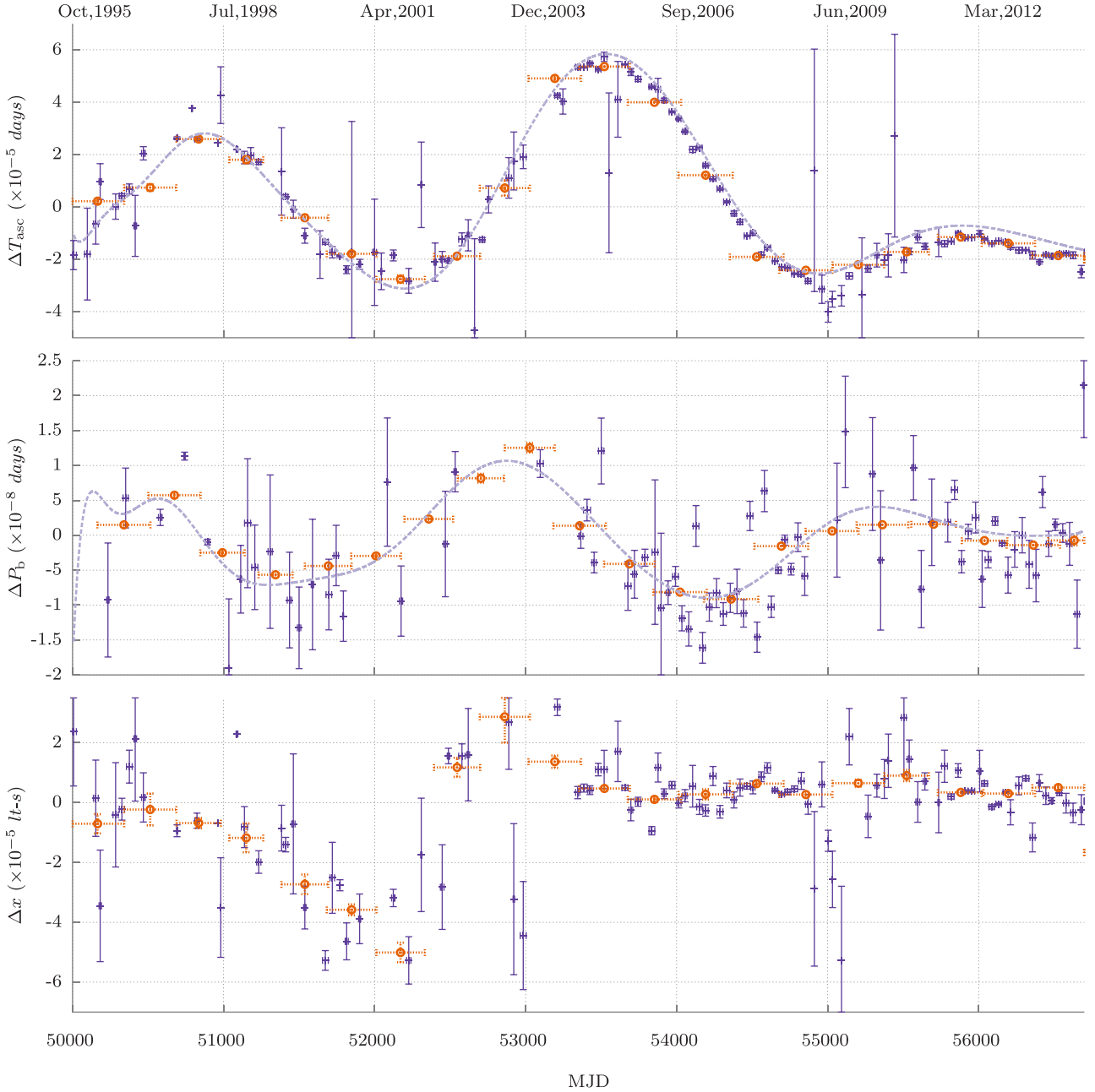
**Figure 5.** Plot of $\Delta T_{asc}$, $\Delta P_b$ and $\Delta x$ measured from fitting for $x$ and $T_{asc}$ only for epochs with a length of 45 (purple +) and 365 (orange ⊙) days, along with the variations described by the BTX model (lilac, dashed). To improve the readability of the graphs for $\Delta P_b$ and $\Delta x$, points with uncertainties comparable to the *y*-range of the graph (typically in the earliest epochs) are removed. The prominent fluctuations for the BTX prediction of $\Delta P_b$ at ~MJD 50100–50600 agree with the measured (but unplotted) values, as can be discerned from the $\Delta T_{asc}$ plot.

A more robust analysis is performed by reducing covariant terms, and it is shown that the resulting measurements are more precise and consistent with earlier analyses. The variations of the orbital period are detected over more than a full 'period', supporting earlier analyses that suggested that these variations arise from cyclic variations in the companion, instead of a tertiary star or planet. In addition, small-scale fluctuations in the $P_b$ variations are detected.

The continued timing of PSR J2051−0827 shows that the variation of the projected semi-major axis appears to have decreased and does not show the extreme behaviour observed at an earlier epoch, lending hope that the black-widow system containing PSR J2051−0827 may be included in PTAs in the near future.

**Table 5.** Maximum contributions from the various sources of secular variations in $P_b$ and $x$ as presented in equations (2) and (3).

| Source | $\dot{P}_b$ (days) | $\dot{x}$ (lt-s) |
|---|---|---|
| GW emission | $-7.61 \times 10^{-14}$ | $-2.67 \times 10^{-19}$ |
| Doppler correction | $-4.06 \times 10^{-21}$ | $-4.06 \times 10^{-21}$ |
| Proper motion corr. | N/A | $4.99 \times 10^{-17}$ |
| Varying aberration | N/A | $-4.41 \times 10^{-17}$ |
| Mass-loss | Requires unphysical $\dot{m}_c \sim 10^{-7}\,M_\odot$ | |
| Mass/GQ variations | See Lazaridis et al. (2011) | |
| Spin-orbit coupling | See Lazaridis et al. (2011) | |
| Max. measured | $1.41 \times 10^{-11}$ | $2.29 \times 10^{-13}$ |
| Min. measured | $-2.03 \times 10^{-11}$ | $-5.08 \times 10^{-13}$ |

*Notes.* (1) The contribution from gravitational quadrupole (GQ) and the classical spin-orbit coupling variations require assumptions based on Lazaridis et al. (2011). Since the derived values are then identical to those presented there, readers are referred to the original source instead.
(2) $\dot{m}_c$ refers to the rate at which mass is lost by the companion.
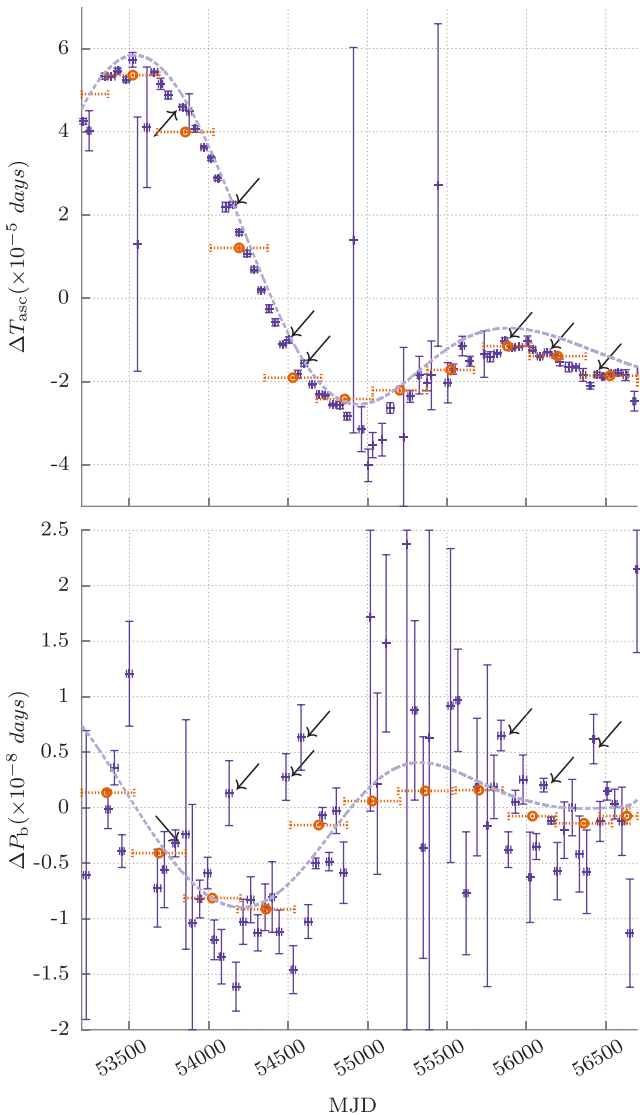


**Figure 6.** Zoomed-in plot of $\Delta T_{\mathrm{asc}}$, $\Delta P_b$ and $\Delta x$ measured from fitting for $x$ and $T_{\mathrm{asc}}$ only for 45 (purple +) and 365 (orange ⊙) day long epochs, along with the predicted variations from the BTX model (lilac, dashed). Solid black arrows indicate epochs where the derivative of $T_{\mathrm{asc}}$ abruptly changes sign.

**REFERENCES**

Abdo A. A. et al., 2013, ApJS, 208, 17
Akaike H., 1974, IEEE Trans. Autom. Control, 19, 716
Applegate J. H., Shaham J., 1994, ApJ, 436, 312
Archibald A. M. et al., 2009, Science, 324, 1411
Bassa C. G. et al., 2016, MNRAS, 456, 2196
Blandford R., Teukolsky S. A., 1976, ApJ, 205, 580
Bochenek C., Ransom S., Demorest P., 2015, ApJ, 813, L4
Chen H.-L., Chen X., Tauris T. M., Han Z., 2013, ApJ, 775, 27
Cordes J. M., Lazio T. J. W., 2003, preprint (arXiv:e-prints)
Demorest P. B. et al., 2013, ApJ, 762, 94
Desvignes G., Barott W. C., Cognard I., Lespagnol P., Theureau G., 2011, in Burgay M., D'Amico N., Esposito P., Pellizzoni A., Possenti A., eds, AIP Conf. Ser. Vol. 1357, Radio Pulsars: An Astrophysical Key to Unlock the Secrets of the Universe. Am. Inst. Phys., New York, p. 349
Desvignes G. et al., 2016, MNRAS, 458, 3341
Doroshenko O., Löhmer O., Kramer M., Jessner A., Wielebinski R., Lyne A. G., Lange C., 2001, A&A, 379, 579
Folkner W. M., Williams J. G., Boggs D. H., 2009, Interplanet. Netw. Prog. Rep., 178, C1
Freire P. C., Camilo F., Kramer M., Lorimer D. R., Lyne A. G., Manchester R. N., D'Amico N., 2003, MNRAS, 340, 1359
Fruchter A. S., Stinebring D. R., Taylor J. H., 1988, Nature, 333, 237
Hobbs G. B., Edwards R. T., Manchester R. N., 2006, MNRAS, 369, 655
Hotan A. W., van Straten W., Manchester R. N., 2004, PASA, 21, 302
Joshi K. J., Rasio F. A., 1997, ApJ, 479, 948
Karuppusamy R., Stappers B., van Straten W., 2008, PASP, 120, 191
Kondratiev V. I. et al., 2016, A&A, 585, A128
Lange C., Camilo F., Wex N., Kramer M., Backer D., Lyne A., Doroshenko O., 2001, MNRAS, 326, 274
Lanza A. F., Rodonò M., 2001, A&A, 376, 165
Lazaridis K. et al., 2011, MNRAS, 414, 3134
Lazarus P., Karuppusamy R., Graikou E., Caballero R. N., Champion D. J., Lee K. J., Verbiest J. P. W., Kramer M., 2016, MNRAS, 458, 868
Lentati L. et al., 2015, MNRAS, 453, 2576
Lorimer D. R., Kramer M., 2005, Handbook of Pulsar Astronomy. Cambridge Univ. Press Cambridge
Lynch R. S., Freire P. C. C., Ransom S. M., Jacoby B. A., 2012, ApJ, 745, 109
Ng C. et al., 2014, MNRAS, 439, 1865

Nice D. J., Arzoumanian Z., Thorsett S. E., 2000, in Kramer M., Wex N., Wielebinski R., eds, ASP Conf. Ser. 202, IAU Colloq. 177: Pulsar Astronomy – 2000 and Beyond. Astron. Soc. Pac., San Francisco, p. 67

Roberts M. S. E., 2013, in van Leeuwen J., ed., Proc. IAU Symp. 291, Neutron Stars and Pulsars: Challenges and Opportunities after 80 Years. Cambridge Univ. Press, Cambridge, p. 127

Shemar S. L., Lyne A. G., 1996, MNRAS, 282, 677

Siemens X., Ellis J., Jenet F., Romano J. D., 2013, Class. Quantum Grav., 30, 224015

Stappers B. W., Bessell M. S., Bailes M., 1996, ApJ, 473, L119

Stappers B. W., Bailes M., Manchester R. N., Sandhu J. S., Toscano M., 1998, ApJ, 499, L183

Stappers B. W., van Kerkwijk M. H., Bell J. F., Kulkarni S. R., 2001, ApJ, 548, L183

Stappers B. W. et al., 2014, ApJ, 790, 39

Takata J., Cheng K. S., Taam R. E., 2012, ApJ, 745, 100

Taylor J. H., 1992, Phil. Trans. R. Soc. A, 341, 117

van Straten W., Demorest P., Oslowski S., 2012, Astron. Res. Technol., 9, 237

Verbiest J. P. W. et al., 2016, MNRAS, 458, 1267

Wu J., Kong A., Huang R., Takata J., Tam P., Wu E., Cheng K., 2012, ApJ, 748, 141

This paper has been typeset from a TEX/LATEX file prepared by the author.